Received: 1 October 2021 | Revised: 23 February 2022 | Accepted: 25 April 2022

DOI: 10.1002/cyto.a.24565

BRIEF REPORT

MIFlowCyt

ISAC INTERNATIONAL SOCIETY FOR ADVANCEMENT OF CYTOMETRY

CYTOMETRY Journal of Quantitative Cell Science PART A

Full spectrum flow cytometry and mass cytometry: A 32-marker panel comparison

Maria C. Jaimes[1] | Michael Leipold[2] | Geoffrey Kraker[3] | El-ad Amir[4] | Holden Maecker[2] | Joanne Lannigan[5]

[1]Applications, Cytek Biosciences, Inc, Fremont, California, USA

[2]Department of Microbiology/Immunology, Stanford University, Stanford, California, USA

[3]Technical Applications Support, Cytek Biosciences Inc., Fremont, California, USA

[4]Astrolabe Diagnostics, Fort Lee, New Jersey, USA

[5]Flow Cytometry Support Services, LLC, Alexandria, Virginia, USA

Correspondence
Maria C. Jaimes, Applications, Cytek Biosciences, Inc, 46107 Landing Parkway, Fremont, CA 94538, USA.
Email: mjaimes@cytekbio.com

Abstract

High-dimensional single-cell data has become an important tool in unraveling the complexity of the immune system and its involvement in homeostasis and a large array of pathologies. As technological tools are developed, researchers are adopting them to answer increasingly complex biological questions. Up until recently, mass cytometry (MC) has been the main technology employed in cytometric assays requiring more than 29 markers. Recently, however, with the introduction of full spectrum flow cytometry (FSFC), it has become possible to break the fluorescence barrier and go beyond 29 fluorescent parameters. In this study, in collaboration with the Stanford Human Immune Monitoring Center (HIMC), we compared five patient samples using an established immune panel developed by the HIMC using their MC platform. Using split samples and the same antibody panel, we were able to demonstrate highly comparable results between the two technologies using multiple data analysis approaches. We report here a direct comparison of two technology platforms (MC and FSFC) using a 32-marker flow cytometric immune monitoring panel that can identify all the previously described and anticipated immune subpopulations defined by this panel.

KEYWORDS
Aurora, CyTOF, full spectrum flow cytometry, high-dimensional immunophenotyping, mass cytometry

1 | INTRODUCTION

The desire to deeply profile the immune system and understand its role in disease and therapeutic responses is driving technological advancement. Immunotherapy has offered new opportunities in the treatment of cancer. However, although promising, there have been mixed outcomes among patients [1–3]. The success of immunotherapy is believed to be dependent on individual patient immune responses and their tumor microenvironments [4–8]. The interaction between the immune response and the tumor microenvironment is a complex milieu which requires a deep profiling of the cellular interactions. As these treatment modalities are expensive, the ability to identify specific biomarkers that can provide insights into which patients are likely to have a positive outcome is a valuable resource for informing clinical trials [9–13]. In addition to immunotherapies, identifying key immune biomarkers, as indicators of vaccine efficacy, can inform decisions for prioritizing vaccines for clinical trials. Deep profiling of the immune system can provide a more thorough understanding of

the mechanisms and pathways of immune evasion, whether post-therapeutically or in the natural responses to cancer and infectious diseases [14]. With this level of information, better informed decisions can be made in the identification of new therapeutic targets and the development of new therapeutic modalities [13, 15–17].

The complexity of the human immune response requires the use of technologies that can provide high-throughput in-depth analysis at the single-cell and population levels [10, 18–21]. These technologies are associated with a higher cost and a higher level of expertise to utilize them. As a result, many major academic institutions have established Shared Resource Centers or Core Facilities to provide access to these technologies for investigators who need to evaluate patient immune responses as part of clinical trials, or for biomarker discovery for future therapeutics development or precision medicine decisions [20, 22]. Flow Cytometry, as a high-throughput, high-dimensional, technology, is an ideal platform for evaluating the immune system at the single-cell level and has been used for many years to study a variety of aspects of the immune system [3]. However, as the complexities of the immune system were unraveled, conventional flow cytometers were unable to analyze the number of markers required to fully explore the dynamics of the immune system. This was primarily due to instrument design, limiting the number of fluorescently tagged markers which could be evaluated in a single tube [23–25]. Comprehensive immune profiling by conventional flow cytometry often requires the use of multiple panels in separate tubes to adequately cover the necessary markers, an approach which does not provide a complete picture of the intricacies of marker co-expression in multiple cell populations [26]. Subsequently, the development of mass cytometry (MC), the application of inductively coupled mass spectroscopy (ICP-MS) using metal-tagged antibodies, enabled an increase in the number of parameters, or markers, that could be measured simultaneously [27, 28]. The use of heavy metal tagged antibodies, in lieu of fluorescently labeled antibodies, addressed the fluorescence spectral overlap issues associated with conventional flow cytometers that limited the number of markers which could be measured in a single tube. MC opened up possibilities for assessing the complexity and heterogeneity of immune responses in clinical research, further contributing to our understanding of the role of the immune system in cancer, immunotherapy, vaccine development, and other pathological processes [9, 17, 19, 24, 29–33]. While this technology has been a major breakthrough in providing the ability to expand immune profiling panels beyond 30 markers, it has been primarily restricted to larger shared resource centers and core facilities due to cost, space requirements, and expertise required to operate [19, 34, 35]. In recent years, the development of commercial instrumentation that takes advantage of full spectrum fluorescence has provided the ability to increase the number of possible fluorochromes that can be effectively used together in a single panel [22, 36–42]. Full spectrum flow cytometry (FSFC) measures the entire fluorochrome emission spectrum, across multiple lasers and using many more detectors than a conventional flow cytometer, allowing a specific spectral fingerprint to be defined for each fluorochrome. FSFC distinguishes one fluorochrome from another using the spectral fingerprint as a unique identifier. This contrasts with using a fluorochrome's maximum emission wavelength, which is what is done on a conventional flow cytometer, to define a fluorochrome. The use of the spectrum outside of the maximum emission enables the use of fluorochromes which have similar maximum emissions profiles but differ in other areas of the spectrum across multiple lasers. The combination of this different approach from the optics perspective as well as a different mathematical approach to identify the signal specific from each fluorochrome results in an extremely flexible system that allows the use of highly overlapping dyes without sacrificing resolution. Leveraging FSFC technology, the ability to combine 30–40 fluorescently labeled antibodies, in a single tube, has been demonstrated using a fluorescence-based flow cytometer [2].

In this study, we chose to evaluate whether a published immune monitoring panel that was established using MC [43, 44] could be replicated using FSFC. The value of FSFC as a powerful technology for cancer immunotherapy has been previously described [22, 45]. There are several advantages and disadvantages to each technology, which are outlined in Table 1; however, the main purpose of this study was to establish the feasibility of generating comparable data with both technologies using a panel previously validated with MC. Since the workflow on a FSFC is very similar to most conventional flow cytometers in terms of instrument operation, acquisition, and maintenance, many researchers should be able to easily adopt this technology. This would enable broader access to high-dimensional immunophenotyping for those wishing to investigate the complexities of the immune system with a single panel and smaller sample requirements.

A recently published study [46] compared data from a panel of 20 markers using an Aurora FSFC (Cytek Biosciences, Fremont, CA) and a CyTOF MC (Fluidigm, S. San Francisco, CA) and found both technologies produced comparable results. In this study, we expand the comparison to an established 32-marker immune monitoring panel on peripheral blood mononuclear cells (PBMCs) using an Aurora FSFC and a Helios MC to demonstrate the ability to use FSFC as another option for monitoring complex immune responses.

2 | MATERIALS AND METHODS

2.1 | Donors

Frozen PBMCs from 5 donors were obtained from AllCells Alameda (Alameda, CA). Cells were provided aliquoted in 25 million cells per vial in freezing media and cryopreserved in liquid nitrogen until ready to use. Ethical review and regulatory compliance were conducted at AllCells by Alpha Independent Review Board under Protocol number: 7000-SOP-045 (effective through April 2, 2023).

2.2 | MC panel design, staining procedure, and sample acquisition

The MC surface marker staining panel (Table S1) was inspired by the HIPC Lyoplate cocktails [47], collapsing most of the markers in the

TABLE 1 Comparison of mass cytometry and full spectrum flow cytometry.

Feature	MC	FSFC	References
Number of markers demonstrated[a]	43	40	[2, 73]
Signal detected	Metal isotopes	Fluorescent probes	[27, 28]
Directly conjugated antibody availability	Single vendor	Many vendors	[34]
Sensitivity limit	300–400 molecules	<40 molecules	[34, 48]
Autofluorescence	No	Yes[b]	[14, 38]
Throughput	500 cells/s	10–15,000 cells/s	[34, 74]
Cell transmission efficiency	30%–60%[c]	>95%	[19, 34]
Cell size/complexity directly measured	No	Yes	[74, 75]
Single label controls required	No	Yes	[39]
Cell sorting	No	Yes	
Normalization of data post-acquisition	Yes	No	[76]

Abbreviations: FSFC, full spectrum flow cytometry; MC, mass cytometry.
[a]Does not include bar-coding, includes live/dead.
[b]Can be extracted for increasing resolution as well as used as an additional parameter for analysis.
[c]30% for earlier MC models; 50%–60% for later MC models.

five fluorescent flow panels into a single MC panel and then adding additional markers. All antibodies were from purified, unconjugated, carrier-protein-free stocks from BD Biosciences, BioLegend, or R&D Systems. For the in-house conjugations, the DN3 polymer was from Fluidigm and metal isotopes were from Fluidigm, Trace Sciences, or Sigma. Mass cytometers have a mass-dependent sensitivity profile [48], with the highest sensitivity in the 159–175 mass range. The choice of metal labeling with each antibody was chosen according to marker expression, with higher-expressing markers generally receiving "dimmer" metals and lower-expressing markers generally receiving "brighter" metals. Additionally, spillovers due to oxide formation (M into the M + 16 channel), isotopic purity, and abundance sensitivity were also addressed [49].

PBMC samples were each thawed in 10 ml RPMI containing 10% heat-inactivate FBS, pen-strep-glutamine (100× dilution from stock), and benzonase (1:10,000 dilution from stock) (complete RPMI) that was pre-warmed to 37°C, then pelleted by centrifugation (480 × g, room temperature, 10 min). The samples were resuspended in 10 ml fresh complete RPMI and re-pelleted. The cell pellet was resuspended in 1 ml CyFACS buffer (1× Rockland PBS/MilliQ supplemented with 2% BSA, 2 mM EDTA, and 0.1% sodium azide), and viable cells were counted by Vicell. Cells were added to a round-bottom 1 ml well microtiter plate at 1.5 million viable cells/well and washed once by pelleting and resuspension in 500 µl fresh CyFACS buffer. The cells were stained for 60 min at room temperature with 50 µl of the antibody-polymer conjugate cocktail (Table S1). The cells were washed twice by pelleting and resuspension with 500 µl CyFACS buffer. The cells were resuspended in 100 µl 1× PBS/MilliQ buffer containing 1.7 µg/ml Live-Dead (diluted 3000× from 5 mg/ml stock DOTA-maleimide [Dojindo] containing natural-abundance indium from Sigma). The cells were washed adding 500 µl CyFACS and pelleting by centrifugation. The cells were resuspended in 100 µl 2% PFA (Electron Microscopy Sciences, 16% methanol-free stock) in Rockland PBS/MilliQ and placed at 4°C overnight.

The next day, 500 µl of CyFACS was added and the cells were pelleted (800 × g, 4°C, 10 min). The cells were resuspended in 100 µl eBiosciences permeabilization buffer (1x in Rockland PBS/MilliQ) and placed on ice for 45 min before 500 µl CyFACS was added, and cells pelleted. The cells were resuspended in 100 µl iridium-containing DNA intercalator (1:2000 dilution in Rockland PBS/MilliQ; Fluidigm) and incubated at room temperature for 20 min, then 500 µl CyFACS was added, and the cells pelleted. The cells were washed twice more in 500 µl MilliQ water. The cells were resuspended in MilliQ water containing 0.1× EQ normalization beads (Fluidigm) to a concentration of 0.7–0.8 million/ml (Bio-Rad TC20 measurement) before acquisition on the Helios mass cytometer (Fluidigm) at a rate of 200–300 events/s. A target number of 250,000 events was acquired per sample (~20 min acquisition time/sample). The samples were acquired immediately after the completion of staining and were not stored.

The Helios mass cytometer was prepared for acquisition by igniting plasma, then running Wash Solution (Fluidigm) for 15 min and Tuning Solution for 5 min before performing a Full Tuning protocol (after 20 min total of warmup time). All tuning values (including Tb159 and Tm169) were within 10% of historical values (see Table S2 for precise values). The Tuning Solution was removed by running Wash Solution for 5 min, then MilliQ water for 5 min, before samples were run. Between each sample, at least 3 min of MilliQ water was run, until the residual event rate in Preview was under 10 events/s. Every 3 samples, 3 min of Wash Solution was run followed by 3 min of MilliQ (until the streaks from the zirconium impurity in Wash Solution could no longer be seen). At the end of all samples, Wash Solution was run for 10 min until all lanthanide signals were at background levels, then MilliQ water was run for 10 min before shutting down.

2.3 | Full spectrum flow cytometry panel design, staining procedure, and sample acquisition

Using the markers included in the MC panel (Table S1), we proceeded to design an equivalent panel to run on a FSFC (Cytek Aurora) equipped with five lasers. The optical configuration of this instrument and the strategy used for the panel design and optimization were as described in OMIP-069 [2]. Briefly, 32 fluorochromes were selected based on their spectral characteristics, ensuring that all had a unique full spectrum signature and could be distinguished from each other. Fluorochrome brightness of each dye, and spread (measured using the spillover spread matrix [50]), were the two metrics used for panel design. The guidelines previously published for successful panel design were followed [39, 40, 51]. Dimmer fluorochromes were assigned to antigens expressed at high levels and with high level of co-expression with other markers in the panel, ensuring good resolution while minimizing spread. Inversely, antigens expressed at low levels were paired with fluorochromes that are very bright or bright and whose signals were not severely impacted by spread from other fluorochromes assigned to co-expressed markers. The selection of marker/fluorochrome was also aimed at maximizing the use of the same clones included in the MC panel. However, there were some restrictions due to commercial availability of reagents or, in some instances, a different clone was selected because of previous validation in other panels developed for the Aurora (data not shown). The final reagent selection is presented in Table S1. All antibodies used in the panel, as well as the viability dye, were titered for optimal signal-to-noise. Panel performance was carefully evaluated, prior to running the samples for this study, and deemed to be optimal as resolution of each marker was comparable in the single stained versus the multicolor samples (Figure S1B) and all populations of interest were clearly identified.

Cells from the five donors used in this study were stained and acquired on the same day. PBMCs were thawed following the same procedure described for the MC panel. However, differently to the MC procedure, after the second wash, cells were resuspended in 7.5 ml of complete RPMI (approximate concentration 3 million/ml). From each donor, 700 µl of cell suspension were transferred to a 12 mm × 75 mm tube labeled with the donor ID + Multicolor. In addition, from one of the donors, 300 µl of cell suspension were transferred to 32 12 mm × 75 mm tubes, each labeled with the name of a marker/fluorochrome pair. For each donor, one unstained control tube was prepared, and in addition to inclusion in the multicolor sample, cell viability was assessed prior to doing the staining with the full cocktail by staining with the amine reactive viability dye LIVE/Dead Blue (Thermo Fisher). All donors had viability higher than 90%. Single stained cells were stained for 30 min at room temperature with optimal titer for each antibody. For the multicolor tubes (one for each donor), cells were first washed with 1x PBS, stained with optimal titer of the viability dye for 15 min, washed with BD Stain Buffer (BSA, BD Biosciences) and then stained for 30 min with the antibody cocktail in presence of Brilliant Staining Buffer (BD Biosciences). After staining was completed, cells were washed once by pelleting with the BD Stain Buffer and then resuspended with 500 µl of 1% PFA. Cells were incubated for 30 min and then washed by pelleting and resuspended in 350 µl of BD Stain Buffer.

Prior to acquisition, instrument set up and Quality Control for the FSFC was performed per the manufacturer recommendations. Single stained controls were acquired first, an unmixing matrix with autofluorescence extraction was calculated using SpectroFlo 2.2.1 and the multicolor samples were run using the live unmixing functionality, setting the stopping criteria using $CD3^+$ cells to achieve, per donor, the same number of events collected in the MC. Samples were run at medium flow rate (averaging 800 events/s for the sample concentration used; ~1.5 million/ml) and the time of acquisition ranged from 2 min 40 s to 3 min and 20 s per sample. Medium flow rate was chosen because it was the highest flow rate that had minimal impact on data resolution.

2.4 | Data QC and manual analysis

For the MC data, after acquisition, the files were normalized together in one batch using Premessa R package (version 0.2.5, RStudio 1.1.456, R 3.3.3). Since no antibody capture bead data was collected, no mass compensation was performed [52, 53]. Manual data analysis was performed using FlowJo v10.1r5 by gating on Ir191 versus Ce140 ("Cells" $Ir191^+Ce140^-$), then Ir191 versus Ir193 ("Intact Cells" $Ir191^+Ir193^+$), then Ir191 versus Event Length ("Intact Singlets" $Ir191^+$ Event Length < ~30), then Ir191 versus Live-Dead In115 ("Live Intact Singlets" $Ir191^+$Live-$Dead^-$), followed by surface marker-based cell subset-specific gating (Figure S1C) modeled after the HIPC Lyoplate panel gating [47]. Samples were evaluated for signal stability using Time versus Ir, CD3, and CD19 (Figure S1A).

The FSFC data was QC'ed using SpectroFlo 2.2.1. NxN plots were used to QC the unmixing accuracy in the multicolor tubes as described in OMIP-069 [2] and corrections were applied when necessary. The largest correction applied was 4.09% (Qdot800 into PE-Cy7). As a best practice, and to demonstrate that the corrections made (with full knowledge of the biology and expected patterns for the markers in this panel) do not impact the results presented in this paper, a dimensionality reduction analysis using data with or without spillover corrections was performed (Figure S8).

Time versus SSC plots were visualized to assess signal stability throughout the acquisition. Examples of signal stability using time versus FSC, CD3, and CD19 plots are presented in Figure S1A. Finally, multicolor data was gated following the same strategy used for the MC data (Figure S1D).

FCS Express 7.04.0014 was used for visual side-by-side comparison of both data sets. Scaling adjustments were made accordingly, based on the data source, that is, arcsinh cofactor 5 for the MC data (which is most commonly used) and biexponential transformation set to ensure all events were displayed off the axes for the FSFC data. Differences in the distribution of the negative populations resulting from contributions of spillover spreading errors between

fluorochromes necessitated fluorochrome-specific biexponential transformation.

2.5 | Analysis using the astrolabe cytometry platform

The Astrolabe Cytometry Platform is a commercially available cloud-based platform for the automated and standardized analysis of flow and MC data [54]. Astrolabe was applied to the autofluorescence extracted FSFC data and bead-normalized MC data. Astrolabe preprocessed the FSFC data using the logicleTransform function from the flowCore package [55] followed by a FSC/SSC gate removing debris and doublets, and a Live/Dead gate removing dead cells. The platform preprocessed the MC data using an arcsinh transformation with a cofactor of 5 followed by a 140/151/165/175 gate removing beads, a DNA/Event Length gate removing debris and doublets, and a In115Di removing dead cells. Astrolabe then labeled 24 canonical cell subsets, mirroring the manual gating strategy proposed for manual gating of the MC data (Figure S1C). The labeling strategy was adapted to the FSFC data by adding SSC in the separation of myeloid and non-myeloid cells.

We inspected marker staining and variability using the average overlap frequency (AOF) [56] to assess staining quality based on a bimodal distribution model of marker intensity and also employed the coefficient of variation (CV) to compare marker intensity noise between the instruments.

2.6 | Unsupervised analysis

Both the FSFC and MC data were analyzed with the OMIQ platform (https://www.omiq.ai/) utilizing the following pipeline. First the scaling was adjusted to ensure at least 99% of events were on scale for each channel and the arcsinh cofactor was set at 6000 to ensure the negative population was unimodal around 0 for the FSFC data and 5 to ensure dim populations were visible for the MC data. The data were gated manually by the manufacturers' recommended strategy to remove doublets, debris, and dead cells and the data were then subsampled to the "clean" population. The flowCut algorithm [57] was used to ensure there was no shift in signal across the time parameter (flowCut settings are as follows: all files used, all fluorescent channels and time selected, Segment = 500, Max Contin = 0.14, Mean of Means = 0.15, Max of Means = 0.22, Max of Valley Height = 0.1, Max Percent to Cut = 0.3, Low Density Removal = 0.1, no Gate Line set, Max Channel for Mean Range = 1, Max Channel for Mean SD = 2, no Flagged Rerun, Uniform of Time Check = 0.22, Remove Multi SD = 7) - all files passed flowCut analysis with the listed settings. Next, a UMAP analysis [46, 58–60] was performed with the following settings to visualize the different sub-populations in distinct groups: all files used, all phenotype parameters used, including ICOS and PD-1, except for CD95 in the FSFC files, Neighbors = 80, Minimum Distance = 0.7, Components = 2, Metric = Euclidean, Learning Rate = 1, Epochs = 250, Seed = 6695 (FSFC) and 1337 (MC), and Embedding Initialization = spectral. After the UMAP analysis, FlowSOM [61] was used to cluster the data. FlowSOM settings for both sets of files are as follows: all files used, clustering features CD16, CD27, CD14, CCR7, CD45RA, CD127, CD28, TCRgd, CD123, CD25, umap_1, and umap_2, 625 clusters with xdim = 25 and ydim = 25, rlen = 10, Distance Metric = Euclidean, Consensus Metaclustering k = 85, Seed = 1531 (FSFC) 7829 (MC). After clustering, the metaclusters were combined into commonly recognized biological populations if they expressed a recognized phenotype. A set of heatmaps was generated comparing the populations that existed in both datasets and a set of plots showing the expression levels of each marker across all UMAP islands is also included. The combination of these methods allows the visualization of unsupervised clustering on the UMAP groups, easy phenotyping of each population via the heatmap, and an easy way to see expression levels of populations on the continuous variable UMAP plots.

3 | RESULTS

The data sets obtained when running the 32-marker panel in each platform, FSFC and MC, were initially analyzed independently to assess data integrity and staining quality. For the FSFC and MC data, signal stability during the acquisition (time vs. parameter) and presence of signal for major markers across all donors were assessed (Figure S1A). While there was some slight signal variation over time in the FSFC data, likely related to the time of the sample boost, the MC data shows more variability, particularly in Donors 5036 and 4392. In addition to variation in MC event rate that are due to micro-clogs from sample quality, there can be a variation in MC event rate due to sample settling in the Pneumatic Sample Introduction (PSI) system. While the PSI does have a stirring mechanism, it may be less efficient than that on the FSFC, especially since MC runs at a slower event rate and therefore has a longer per-sample acquisition time.

For FSFC, unmixed data was evaluated for any obvious unmixing errors that led to visualization artifacts and single versus multicolor data were compared to ensure minimal loss of staining resolution due to spillover spreading (Figure S1B). For the MC data, an internal control was run (Figure S1C) and it was verified that the pattern for all markers was consistent with historical data obtained at the HIMC. We concluded from these steps that both sets of data adhered to quality standards established for each platform and were therefore suitable for comparison.

To perform the comparative analysis of the results obtained in both platforms three approaches were taken. The first approach was to visually compare the data using traditional manual gating, inspecting the data to ensure all expected biologically relevant populations could be identified using the specific markers employed in the panel and to investigate any observations where there were apparent differences in either the qualitative, or quantitative, results between the two platforms. The second approach was to use the Astrolabe Cytometry Platform, a cloud-based service that

automatically identifies canonical cell populations, to do an in-depth quantitative comparison using a standardized method identical between the two data sets. Finally, commonly used, high-dimensional unsupervised algorithm pipelines (FlowSOM and UMAP) were used to further explore similarities, and differences, on the data obtained from these two data sets [46, 58, 59].

3.1 | Manual gating

For manual/visual inspection, the gating strategy established by the authors at the HIMC to QC the MC panel performance was used to assess the ability to identify all expected biological populations for all donor samples acquired on both platforms. The list of markers, and the respective subsets identified by these markers, are provided in Table S1. An example of the gating strategy using representative data from one donor is provided in Figure S1D,E. Scaling adjustments were made as explained in the Methods section. Of note, visual comparison of the data/ patterns needed to consider the difference in distribution of the "negative" populations between the two platforms, that is, lack of negative values in the MC data in contrast to having a population distribution centered around 0 with negative values in fluorescence-based data. In this study, neither the MC nor the FSFC data included Mass Minus One (MMO) [62] or Fluorescence Minus One (FMO) [63, 64] controls respectively, since the subpopulations identified by the markers included in the panel for each platform have been extensively characterized and it had been determined that these were not necessary to establish gate positioning. Internal controls such as differences in pattern or distribution across cell subsets or donors were used, if necessary, to determine gate position. The main goals of the manual gating evaluation of the two data sets were to (1) assess whether the same populations could be identified, starting with the main cellular subsets (monocytes, T cells, B cells, natural killer cells (NKs), and dendritic cells (DCs)), then phenotyping those compartments using the additional markers in the panel, (2) evaluate marker expression patterns and differences across donors, and (3) determine if the ranges of the frequencies of the main subsets for each donor were similar. As there were no replicates of the samples, the differences of population frequencies between the platforms assessed from donor pairs were evaluated qualitatively, not statistically, to identify population differences.

The data from both platforms identified all the expected populations in all donors (Figure S1D,E). Many expression patterns were very comparable between the two data sets, for example the pattern and level of expression of the gamma delta T cells; the expression pattern of CCR7 and CD45RA in $CD4^+$ and $CD8^+$ T cells, allowing for similar identification of naïve, memory, and effector memory subsets; the IgD versus CD27 expression, leading to similar distribution of naïve and memory B cells subsets; and the CD16 versus CD56 patterns in the NK compartment. Importantly, differences in the abundance of a given subset or marker expression patterns across donors were similar on both platforms. For example, and as shown in Figure 1A, in the NK cell compartment, both data sets highlighted differences across donors in the level of expression of both CD161 and CD57, as well as in co-expression between these two markers. In addition, when comparing cellular frequencies in individual donors, there was, for the most part, a high level of agreement between the two sets of data (Figure S2A–E).

We identified, however, patterns that were visually different between the two platforms. For example, the distribution of CD127 and CD25 that allows regulatory T cell (T_{reg}) identification, or the CD38 versus CD24 pattern in B cells, were dissimilar and appear to be related to differences in the resolution/brightness of the antibodies used for CD25 and CD38 respectively (Figure S1D,E). As expected, in cases where staining and population pattern differences were observed through the visual inspection process, differences in the frequencies in the donor pairs were also noted (Figure S3A,B). In general, these differences appeared to be associated with the resolution of the markers defining a specific subpopulation, or markers defining the upstream gates of those subpopulations. In some instances, the differences for some populations/markers were specific to a donor, and not observed across all donors. For example, in donor 5036, the resolution of the $CD14^{+/-}CD33^-$ lineage population was lower in the MC data compared to the FSFC data, and the gating based on these two markers led to major differences in the percentages of downstream populations like $CD20^-$, $CD20^+CD19^+$, and $CD56^{bright}CD16^-$ (Figure S3A). Other donors did not show this level of discordance within these subsets. In contrast, there were several subpopulations that showed similar inconsistencies between the two platforms across multiple donors, and were mainly associated with dimly expressed antigens, such as PD-1 and ICOS, chemokine receptors CXCR5, CCR6, and CXCR3 or CD127 and CD161 expression on T cells. An example of this finding is presented in Figure S3B where the lack of resolution of CXCR5 on non-naïve $CD4^+$ T cells in the MC data on donor 4392 impacts not only the percentage of this population, but also the subpopulations of both the $CXCR5^-$ and $CXCR5^+$ gated populations defined by CXCR3 and CCR6.

The distribution of markers expressed at low levels were assessed in combination with other markers with which they could be co-expressed across different cellular compartments and across all donors. One example of this analysis/visualization strategy is shown in Figure 1B for ICOS. ICOS expression was visualized in all major T cell compartments (B and NK cell compartments had no signal for this marker), allowing clear confirmation of its expression, even if at very low levels. On T cells, co-expression with CD28, and specifically in $CD4^+CD8^-$ T cells, made it easier to visualize and confirm presence or absence of expression. Using this approach, comparison of expression across donors showed similar trends between the two data sets even if there were differences in the frequencies (e.g., donor 4559 had a higher level of expression compared to all other donors).

3.2 | Automated cell subset identification using astrolabe platform

Manual gating depends on an experienced flow cytometrist's extensive knowledge of the biology and staining patterns of the markers employed with regards to setting the thresholds on each marker. This

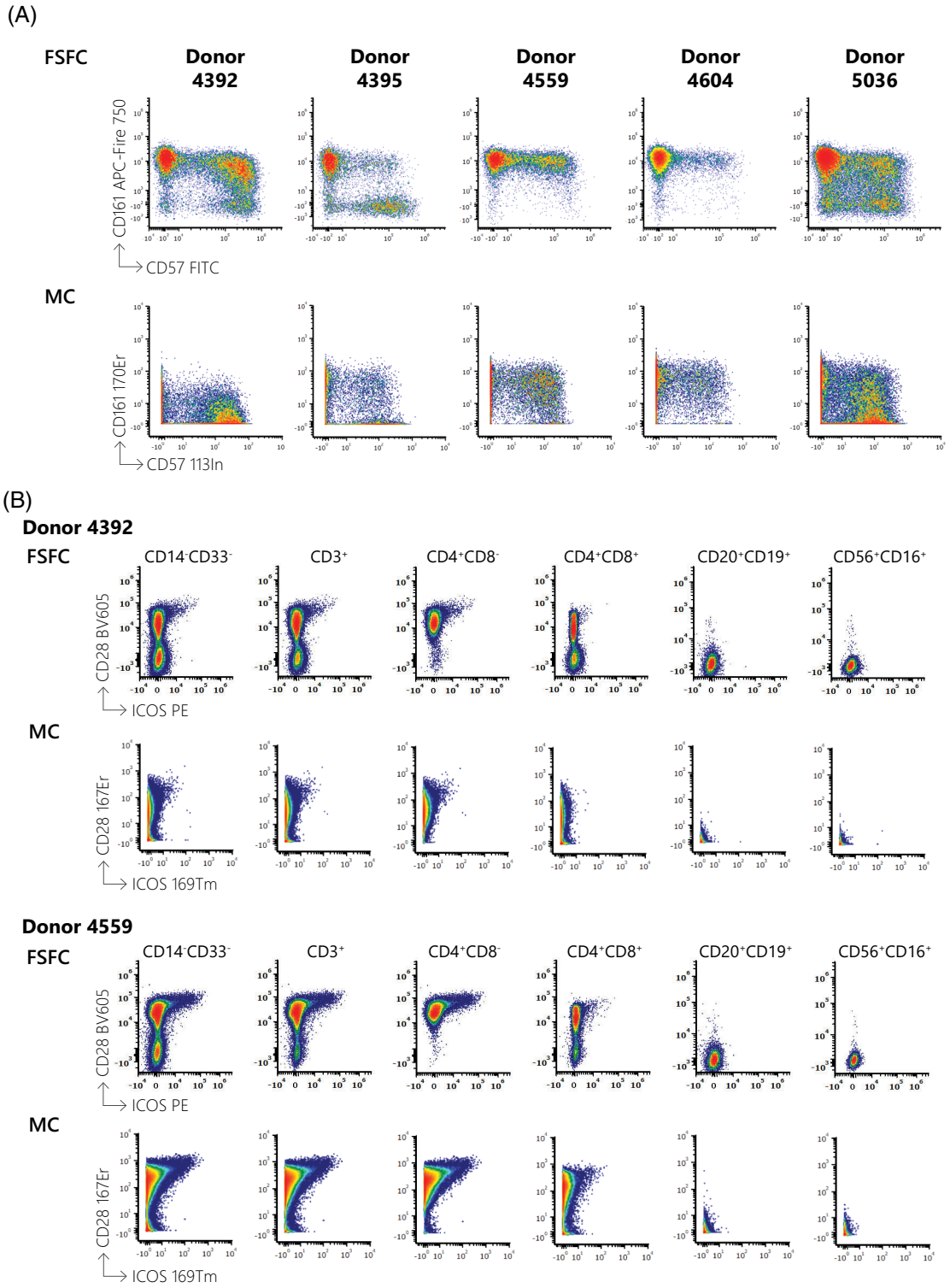

FIGURE 1 Visual comparison of population's patterns and resolution in FSFC and MC data. (A) Dot plots showing CD57 (x-axis) versus CD161 (y-axis) expression in NK cells for all five donors. Data was gated on singlets/lymphocytes/CD14$^-$CD33$^-$/CD3$^-$/CD16$^+$CD56$^+$ as shown in Figure S1D,E. FSFC data (top row), MC data (bottom row). Different levels of expression of both markers across donors following similar patterns in both data sets can be seen. (B) ICOS (x-axis) and CD28 (y-axis) expression across different cell compartments. Data from two different donors is presented, one with low ICOS expression (donor 4392) and one with the highest expression (donor 4559). Each column represents data from a different cell compartment identified based on the gating strategy presented in Figure S1D,E. from left to right: Non-monocytes (CD14$^-$CD33$^-$), T cells (CD3$^+$), CD4 T cells (CD4$^+$CD8$^-$), CD8 T cells (CD4$^-$CD8$^+$), B cells (CD19$^+$CD20$^+$), and NK cells (CD16$^+$CD56$^+$). Note that ICOS was not detected in the B cell and NK cell compartments, allowing the use of those populations to determine the boundaries between ICOS$^+$ and ICOS$^-$ cells in the other compartments. Top row FSFC data, bottom row, and MC data.

could lead to variability across samples, and the possibility of missing relevant subsets which could be identified using a highly complex panel. Moreover, as previously explained, manual gating of the data acquired on the MC and FSFC required using different criteria/strategies to establish the gates as the data presentations and some of the patterns were different. To address the variability and limitations introduced by manual analysis, a second round of analysis was performed using the Astrolabe Cytometry Platform, which is a standardized platform for the analysis of both flow and MC data [54].

The first goal using this analysis pipeline was to assess quantitative differences between the 2 data sets. The frequencies for the major compartment subsets (T, B, NK, NKT, and monocytes) from all cells, across all donors, matched well between the instruments, with Pearson's $\rho = 0.98$ (Figure 2A). Notably, the analysis highlighted an aberrantly high population of NKT cells ($CD3^+CD56^+$) in donor 4395 in both data sets (35% in FSFC, 34% in MC, compared to less than 5% for all other donors) as shown in Figure 2A. This finding was confirmed by examining this subset in the manually gated data (Figure 2B).

Interestingly, if the analysis of the correlation of the cell subset frequencies was done excluding the T cells, to better evaluate cellular subsets with lower frequencies, a lower correlation was found ($\rho = 0.89$) (Figure 3A). It appeared that this could be caused by lower frequencies of NK cells in the MC data compared to the FSFC data. This was confirmed by visual inspection of the plotted data of CD16 versus CD56 in the $CD33^-CD14^-CD3^-$ cells from each instrument (Figure 3B).

We next evaluated the frequencies of subpopulations under the major canonical compartments. High correlation values were obtained when examining subsets within the T cell (CD4 and CD8 naïve/memory cells) ($\rho = 0.97$) (Figure 4A) and NK cell ($\rho = 0.99$) compartments (Figure 4B). For subsets in the B cell compartment, the correlation is also high ($\rho = 0.99$). However, the data generated with the FSFC had a higher frequency of transitional ($CD3^-CD19^+CD20^+CD38^+CD24^+$) B cells in all donors (Figure 4C). We investigated this finding by reviewing the data visualization and manual gating. Because clear identification of this subset relies on optimal CD38 resolution, we compared this marker's expression pattern and resolution on B cells ($CD3^-CD19^+CD20^+$) and NK cells ($CD3^-CD20^-$). However, we did not observe any significant differences that could lead to the discrepancy seen in the frequencies (Figure S4A,B). As CD24 also plays a major role in defining this subset, we then compared the level of CD24 expression in the context of CD38 expression to determine whether the combined expression levels were different between the two platforms. As can be seen in Supplemental 4C, there is a decrease in the staining of CD24 across all donors (with varying degree) in the MC data, not only compared to the FSFC data, but also when compared to the MC QC sample staining. Note that the percentage of transitional B cell in the MC QC sample is in-line with the values obtained with the FSFC data. This reduction in the CD24 staining in

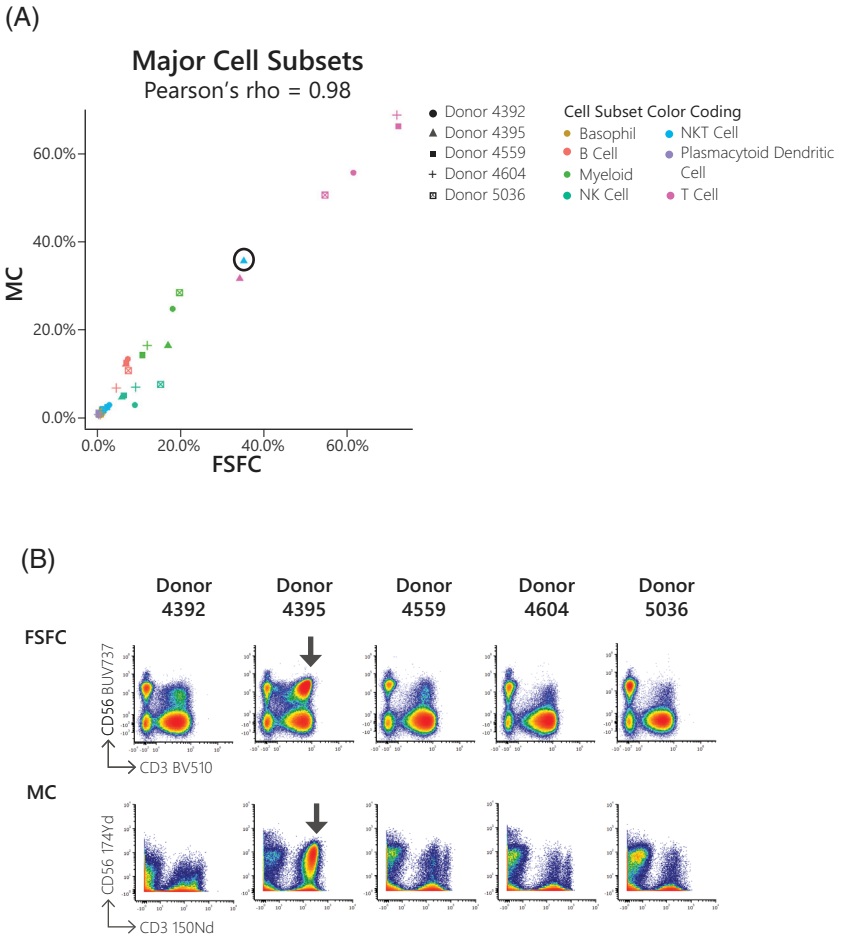

FIGURE 2 (A) Correlation of major cellular subsets frequencies based on analysis using the astrolabe cytometry platform. Frequencies of basophils (light pink), B cells (yellow), monocytes (green), NK cells (light green), NKT cells (blue), plasmacytoid dendritic cells (purple), and T cells (pink) from FSFC (x-axis) compared to MC (y-axis) across all donors (4392 circle, 4395 triangle, 4559 square, 4604 cross, and 5036 crossed square). A high frequency of NKT cells was identified in donor 4395 (blue triangle circled) in both sets of data. (B) Dot plots gated on singlets/live/$CD14^-CD33^-$ cells showing CD3 (x-axis) versus CD56 (y-axis) for all five donors. NKT cells were identified as $CD3^+CD56^+$. A very high frequency of those cells was observed in donor 4395, in contrast to what was seen in other donors, confirming the findings from the astrolabe analysis.

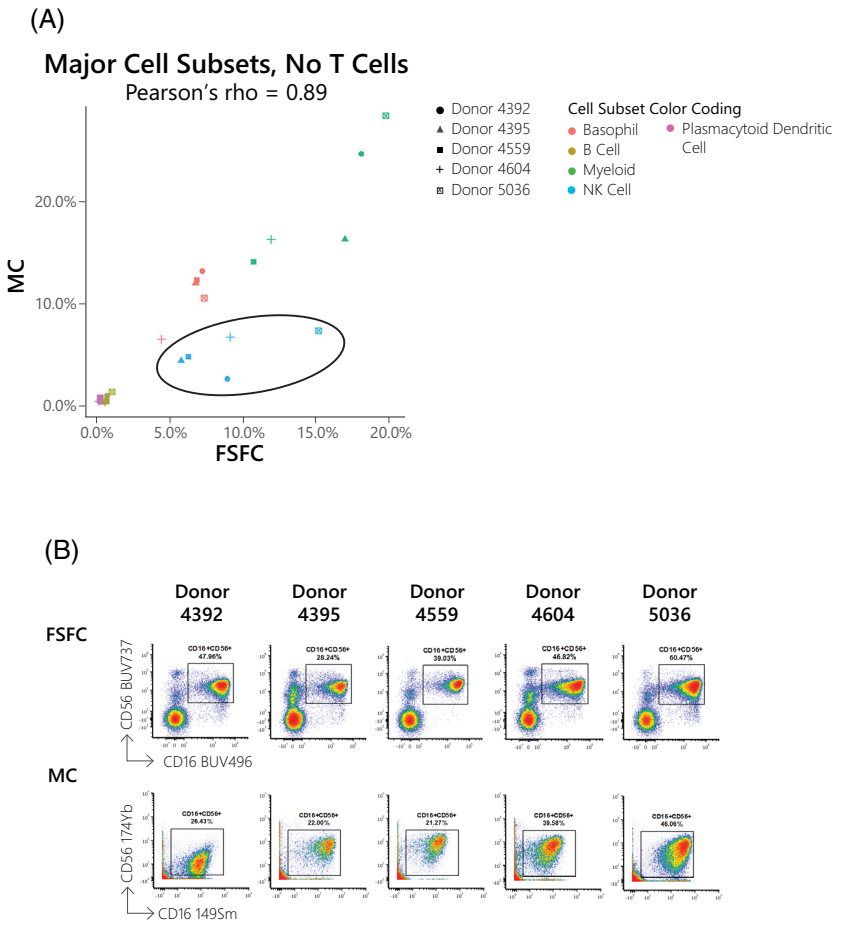

FIGURE 3 (A) Correlation of lower frequency non-T cell subsets frequencies based on analysis using the astrolabe cytometry platform. Frequencies of basophils (light pink), B cells (yellow), monocytes (green), NK cells (blue) and plasmacytoid DCs (pink) from FSFC (x-axis) compared to MC (y-axis) across all donors (4392 circle, 4395 triangle, 4559 square, 4604 cross, and 5036 crossed square). Lower correlation of frequencies of NK cells between the platforms (offset from the diagonal) as indicated by the blue symbols circled in the graph. Higher frequencies were detected in the FSFC compared to the MC. (B) Dot plots showing classical NK cells ($CD16^{+}CD56^{+}$) gated on singlets/live/$CD14^{-}CD33^{-}/CD3^{-}$ cells for all five donors, which represent the low correlations seen in Figure 3A.

the MC data appears to have contributed to the differences in the percentage of transitional B cells. Of note, the approach that was taken for the manual gating strategy was to keep the gate positioning static across samples. Another approach would have been to adjust the gate positioning for each donor to better account for differences in levels of expression that could have led to differences in the percentages reported in Figure S4C. However, the discrepancies obtained from the Astrolabe analysis are independent of these different manual gating strategies.

In contrast to the high correlation observed in T, B, and NK cell subsets, the correlation for myeloid compartments was very low for all donors ($\rho = 0.27$) (Figure 5A). This result confirmed previous observations made during the manual gating of the data. In the MC data the resolution of CD14 and CD16 in monocytes, that were identified as $CD33^{+}$ cells, exhibits a very different pattern for the classification of classical, non-classical, and intermediate subsets compared to the FSFC data (Figure 5B).

3.3 | Staining quality assessment using average overlap frequency analysis

To assess the differences in staining quality and population resolution from the manual gating observations, we chose to use the Average Overlap Frequency (AOF) metric. AOF is an efficient semi-quantitative metric to evaluate and quantify the robustness of staining [56]. AOF models marker distributions as bimodal. In other words, it assumes clear positive and negative peaks. For each (sample, marker) pair, the metric can range between 0% and 100%, where 0% indicates good resolution between positives and negatives, and a decrease in this separation will lead to % increases. Based on the original AOF paper (Figure 2C in Ref. [56]), the AOF threshold was set at 15%, which was the highest reported AOF in that study in which the positive population was still resolvable. Markers above the 15% threshold are flagged as having potential staining/resolution issues. Potential reasons for a high AOF include: (a) sample staining or reagent issue, (b) clustering algorithm issue, (c) biological expression of the marker is continuous (there is no distinct positive peak), and (4) the marker identifies a rare population which the metric could not identify. Manual validation of results is required before making any conclusive decisions regarding data quality using this method. The results of the AOF measurement for every marker included in this panel across all donors are presented as a heatmap in Figure 6A. We found that AOF values were qualitatively similar between the two data sets and that dim markers (PD-1 and ICOS primarily) that did not have a clear positive population were flagged, as expected. To identify potential discrepancies, we examined the AOF correlation across all samples and all markers between the data sets (Figure 6B). This analysis indicated that, overall, there was a good correlation ($\rho = 0.88$), but for certain markers in specific donors there were significant discrepancies. To

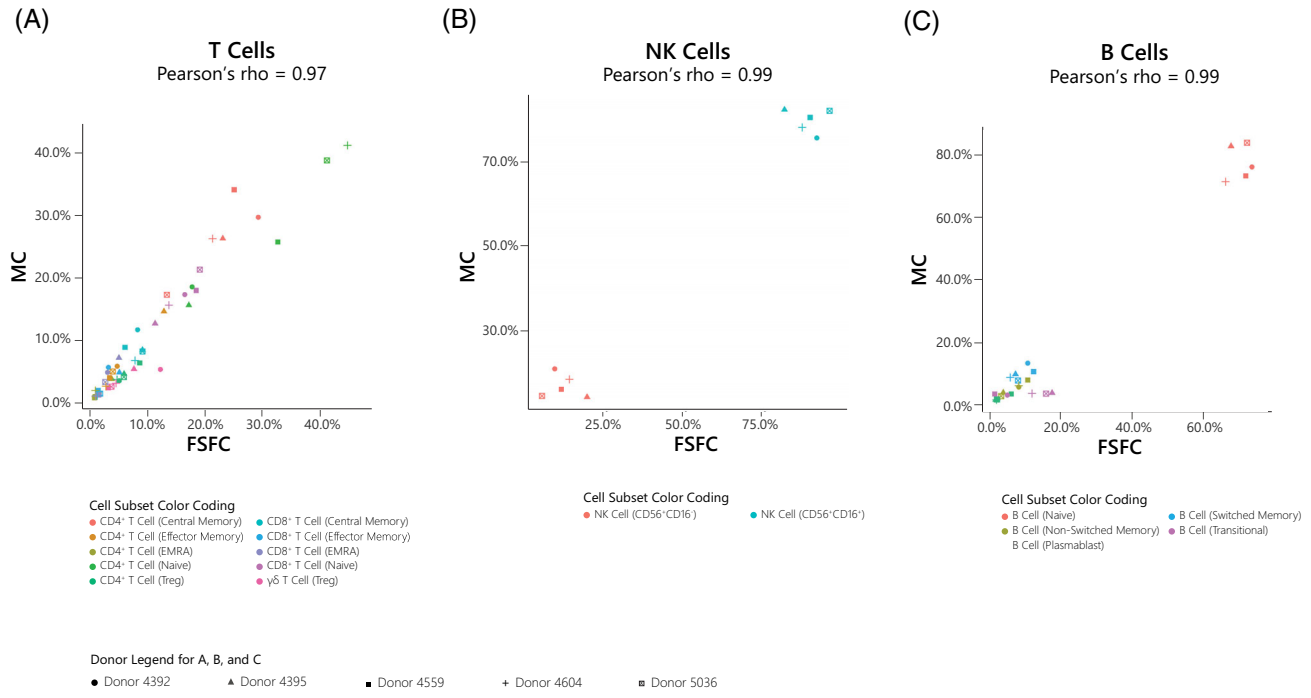

FIGURE 4 Correlation of frequencies of subsets from the T, NK, and B cell compartments based on analysis using the astrolabe cytometry platform (A) memory/effector $CD4^+$ and $CD8^+$ T cell subsets, gamma delta T cells, and regulatory T cells. (B) NK cell subsets ($CD16^+CD56^+$ and $CD16^-CD56^{high}$). (C) Naïve, non-switched memory, switch memory and transitional B cells subsets and plasmablasts. Note the low correlation in the frequencies detected by both platforms for transitional B cells (pink symbols).

FIGURE 5 (A) Correlation of frequencies of myeloid subsets based on analysis using the astrolabe cytometry platform. Frequencies of dendritic cells (red), non-classical ($CD14^-CD16^+$, green), transitional ($CD14^+CD16^+$, purple), and classical ($CD14^+CD16^-$) monocytes identified in the FSFC (x-axis) compared to MC (y-axis) across all donors (4392 circle, 4395 triangle, 4559 square, 4604 cross and 5036 crossed square). This analysis revealed very low correlation for all the myeloid subsets across all donors. (B) Dot plots gated on singlets/live/$CD14^+CD16^+$ showing CD14 (x-axis) versus CD16 (y-axis) for all five donors, demonstrating lower resolution of monocyte subsets in the MC data, likely contributing to the discrepancy in the frequencies of these subsets in the astrolabe analysis.

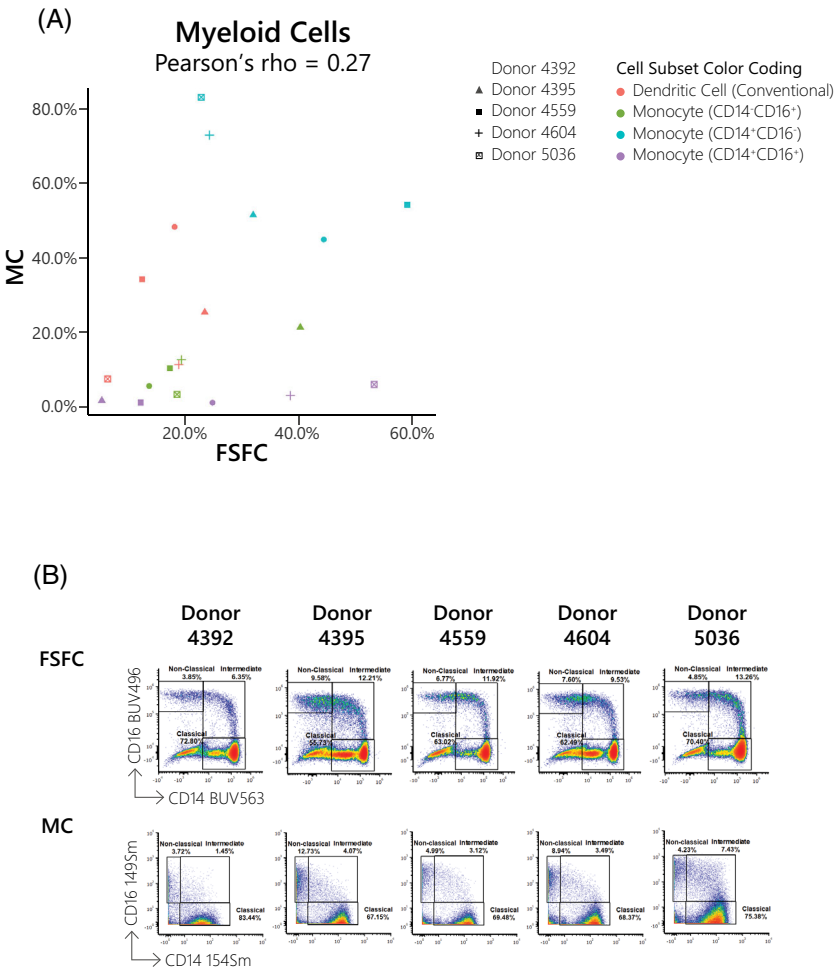

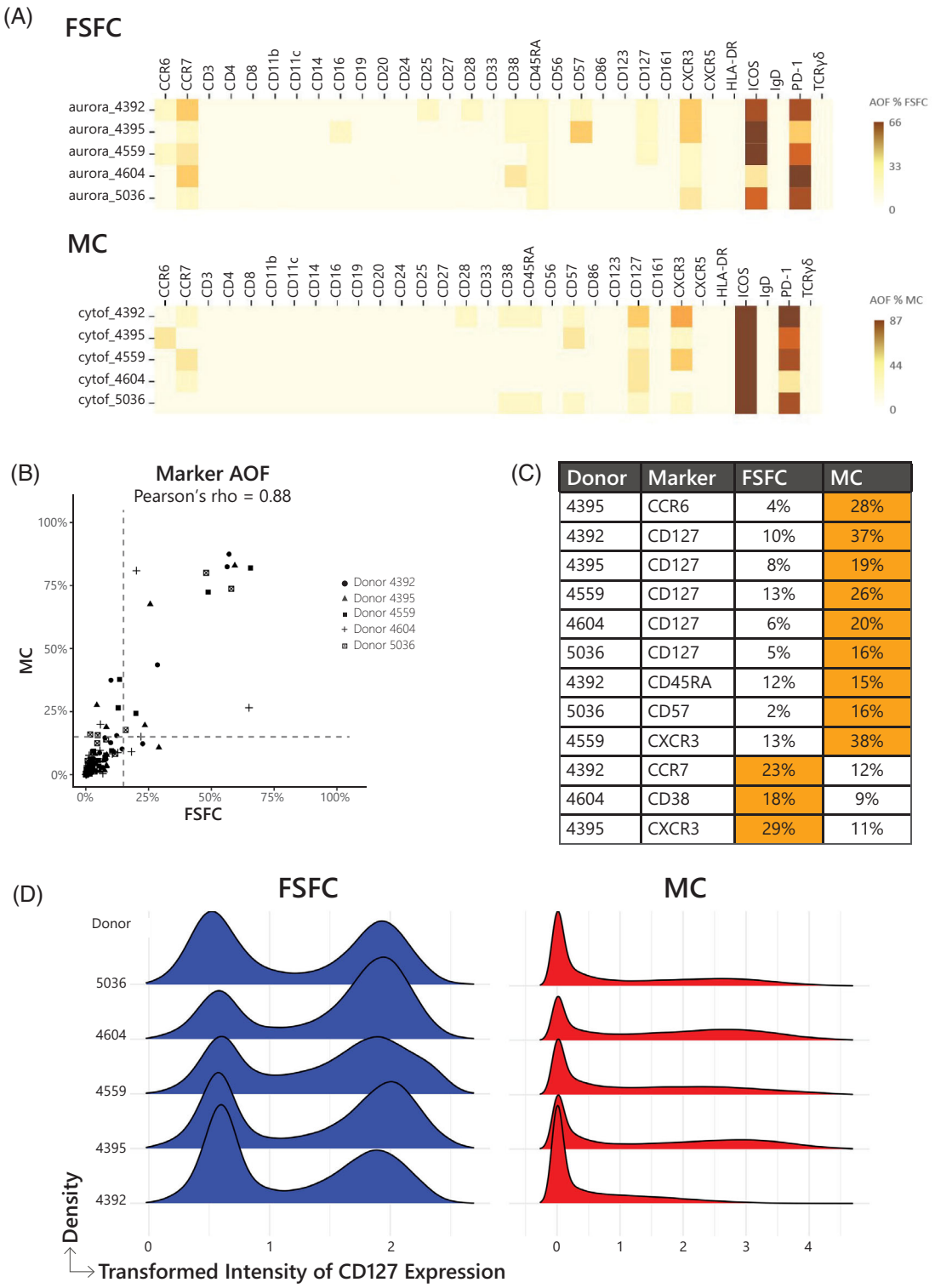

Donor	Marker	FSFC	MC
4395	CCR6	4%	28%
4392	CD127	10%	37%
4395	CD127	8%	19%
4559	CD127	13%	26%
4604	CD127	6%	20%
5036	CD127	5%	16%
4392	CD45RA	12%	15%
5036	CD57	2%	16%
4559	CXCR3	13%	38%
4392	CCR7	23%	12%
4604	CD38	18%	9%
4395	CXCR3	29%	11%

FIGURE 6 Average overlap frequency (AOF) analysis. (A) Heatmap showing AOF for all markers included in the panel (columns) across every donor (rows) for the FSFC (top) and the MC (bottom) data. Low AOF (light colored cells) indicate good resolution of the positive population whereas high values (dark cells) indicate poor resolution. Note the high level of agreement of AOF values between the two data sets. (B) High correlation between AOF values from FSFC (x-axis) versus MC data (y-axis), ($\rho = 0.88$). (C) List of sample and marker pairs that are below the 15% threshold for one instrument but above that value for the other. Orange denotes greater than 15%. (D) Comparison of CD127 distributions between the two instruments. For a direct comparison the data intensity was normalized (x-axis, transformed intensity) as well as the cell frequency (y-axis, density). In the FSFC data the distribution is bimodal with a strong positive peak. On the other hand, in the MC data the positive peak is more of a smear, especially in donor 4392.

further examine these discrepancies, the sample and marker pairs that were below the 15% threshold for one instrument but above that value for the other were evaluated. These values are summarized in the table in Figure 6C, where orange denotes greater than 15%. Upon closer manual inspection, several markers have consistent differences in distribution between the instruments. For example, the distribution for CD127 (Figure 6D) in the FSFC data is bimodal with a strong positive peak. On the other hand, in the MC data the positive peak is more of a smear, especially in donor 4392. Two other markers that exhibited a similar trend were CCR6 and CXCR3. As can be seen in Figure S5, the CCR6 and CXCR3 markers in the FSFC data exhibited a clearer positive/negative distribution across all donors compared to the MC data.

3.4 | Quantitative marker variability comparison

AOF assesses staining quality based on the bimodal distribution assumption. To approach potential variability assuming a continuous distribution, we utilized the coefficient of variation (CV), which is

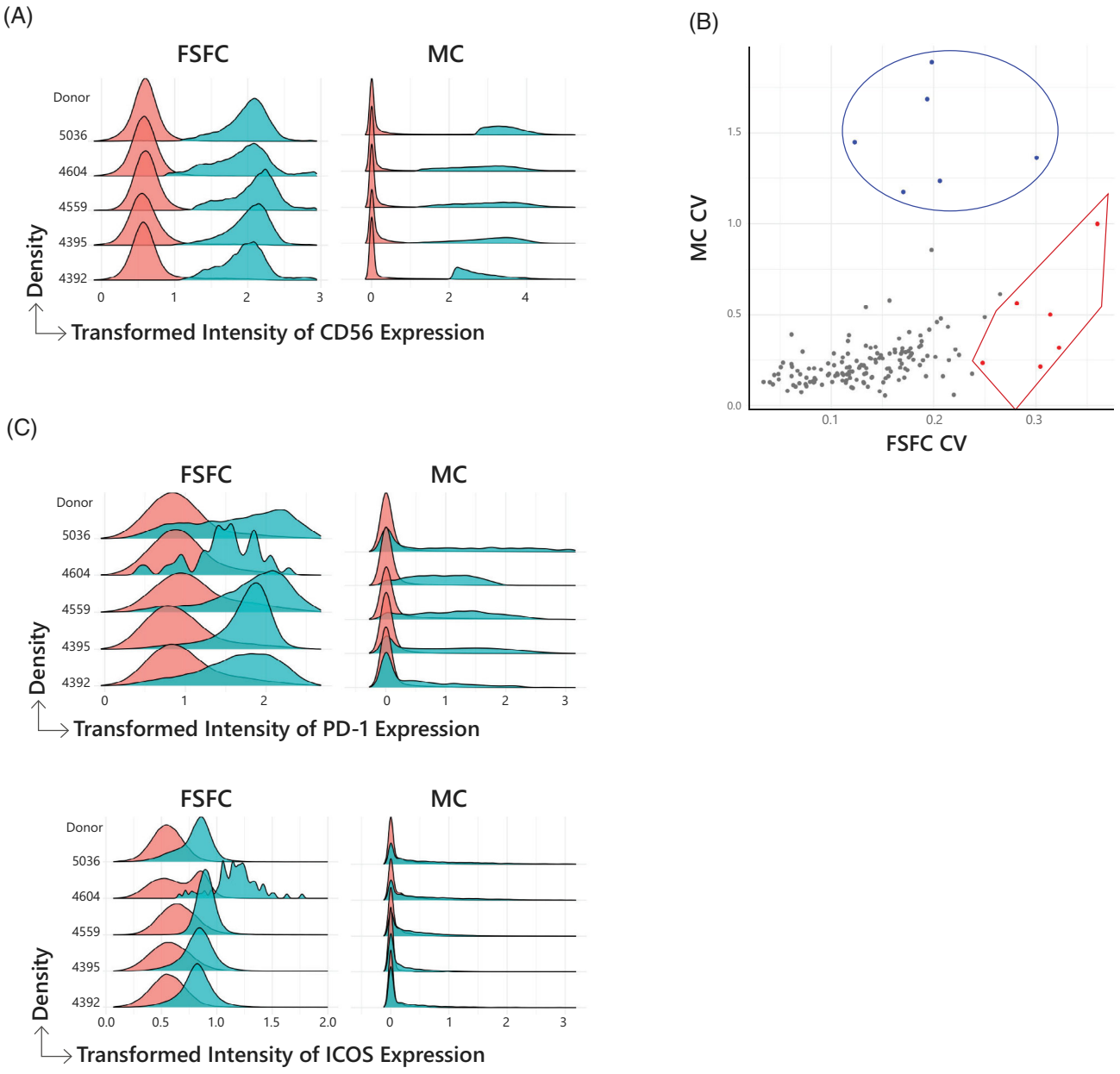

FIGURE 7 Coefficient of variation (CV) analysis. (A) Comparison of CD56 distribution between the two instruments. Data was normalized as in Figure 6D. (B) Scatter plot comparing the coefficient of variation (CV) between the FSFC (x-axis) and MC (y-axis). Every dot is a (donor, marker) pair. A linear regression model was fit to the data to identify outliers (red and blue dots, respectively). (C) Comparison of PD-1 (top) and ICOS (bottom) distribution between the two instruments. Data was normalized as in Figure 6D.

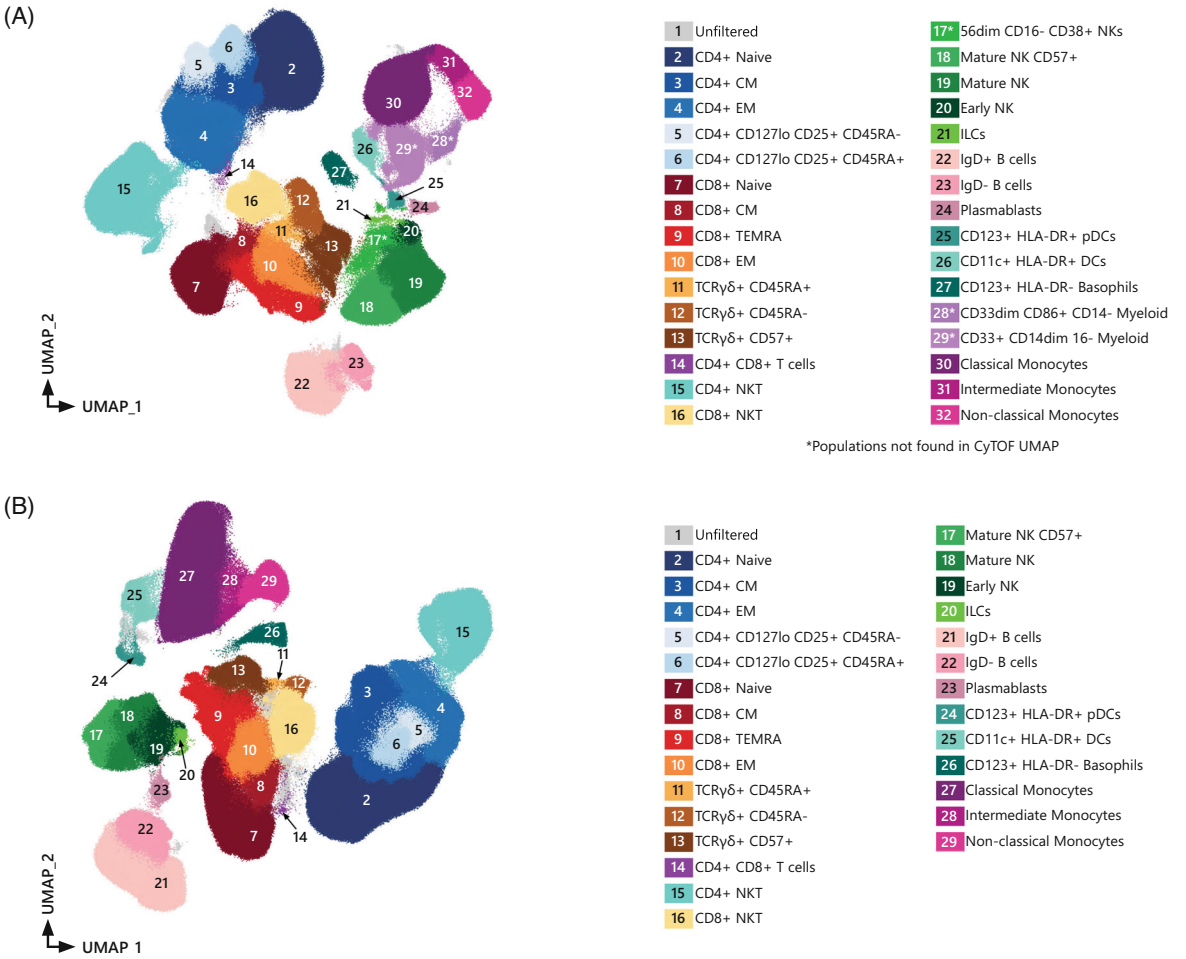

FIGURE 8 Algorithm assisted high-dimensional analysis on PBMCs from five concatenated donor samples acquired on either FSFC (A) or MC (B), displaying FlowSOM clusters projected on to two UMAP dimensions to visualize concordance between the differing acquisition technologies. Note that 3 additional populations (identified with an arrow) were only identified in the FSFC data. (C) Heatmaps displaying the marker expressions of manually labeled FlowSOM clusters from five concatenated samples. FSFC (top) and MC (bottom). The marker expression intensity is displayed on a scale from white (negative) to blue (positive). Each column's max and min are mapped to this scale, so the values change between markers, consequently the scale is labeled with - and + to indicate relative magnitude. One example of a difference between the two platforms is highlighted by the red boxes. (D) Density colored UMAP plots comparing population distribution in the FSFC (left) versus MC (right) from donor 4395, highlighting the high frequency of NKT cells as previously illustrated in Figure 2.

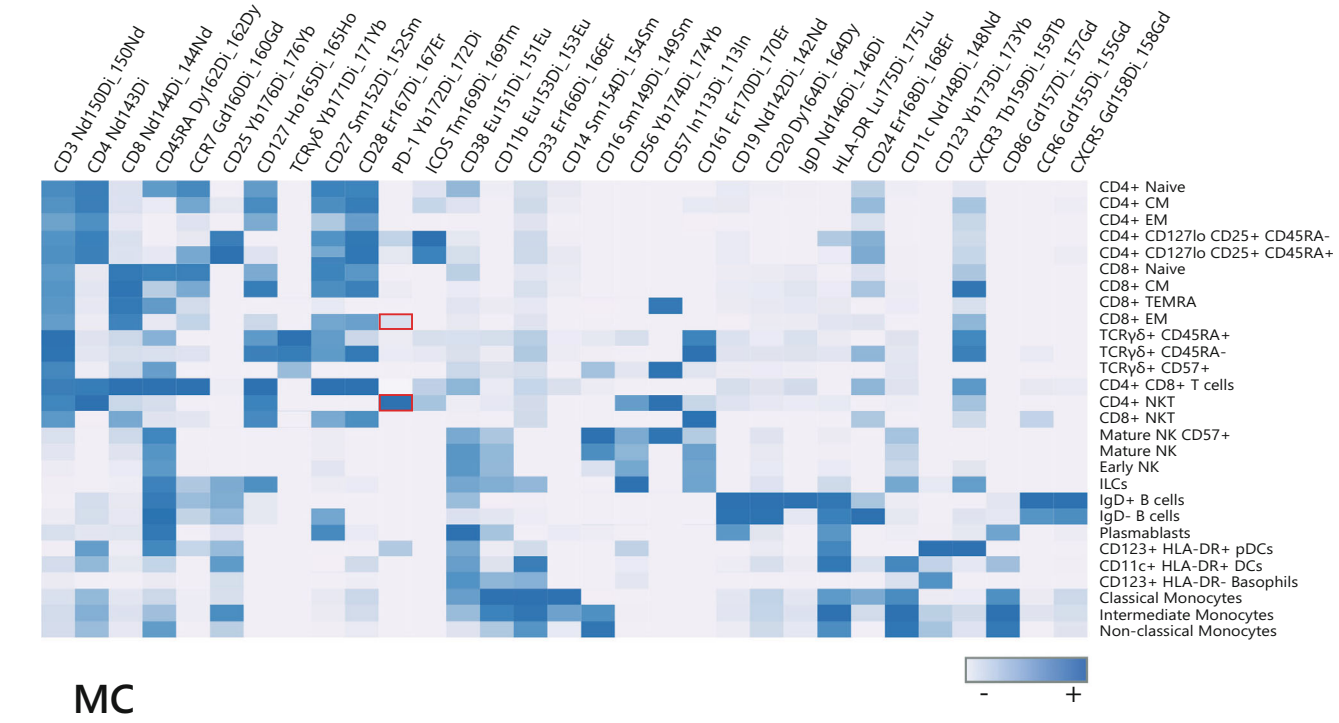

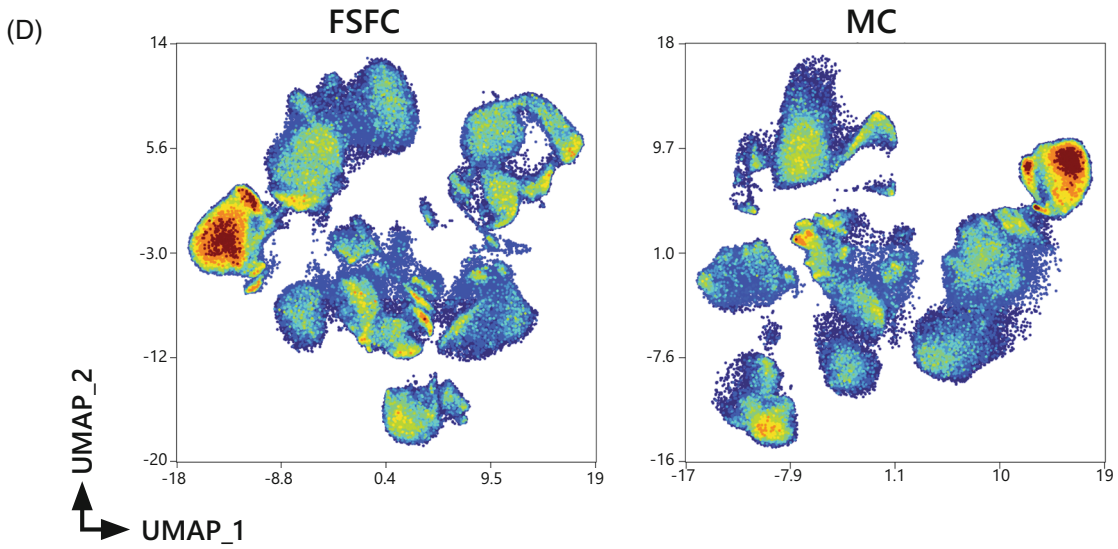

FIGURE 8 (Continued)

defined as the standard deviation divided by the mean. The CV is a standardized measure of dispersion and an accepted measure for biological and technical noise [65].

In the context of the instrument comparison, we calculated the CV for the positive peak of every marker, which was defined based on the AOF, per the methods described in [56]. An example of the visualization of this analysis that allows to identify the positive and negative peaks for each marker, independent of their distribution, in the data for each instrument is presented for CD56 in Figure 7A. We then compared the CVs from each of the data sets using a dot plot, where each dot is the CV of the positive peak of a marker in one of the donors (Figure 7B). Of note, the CV is scale-sensitive, which leads to differences in actual values between the FSFC and the MC. To quantify which (sample, marker) pairs differ between the instruments, we fit a linear regression model between the MC and the FSFC and vice versa. (Sample, marker) pairs with a standardized residual greater than 2 are marked in red (FSFC) and in blue (MC). Out of the 155 pairs compared, six were identified as having higher CVs in the MC data

(blue dots). Those correspond to ICOS in all 5 donors and PD-1 in donor 4392. Both are dim markers and have a spread distribution in the MC data making it challenging to identify a clear positive peak (Figures 1E and 6C).

Another 6 pairs were flagged in the FSFC data (red dots): CD127/donor 4559, CD45RA/donor 4559, CD57/donor 4395, HLA-DR/donor 4395, and PD-1/donors 4604 and 5036. Closer examination and reviewing of the manual gating did not identify any staining issues with these pairs and therefore were classified as false positives (Figure S6).

3.5 | Data analysis using high-dimensional unsupervised pipeline

Our third approach to comparing the performance of this panel between platforms was to utilize an unsupervised algorithm pipeline, as this is likely a common approach to be applied by users of both the FSFC and MC platforms [2, 66]. Dimensionality reduction, combined with clustering algorithms, have been successfully used for the data analysis of complex datasets from both mass and fluorescence cytometry platforms [46, 60, 66, 67]. Here, we chose to use Uniform Manifold Approximation and Projection (UMAP) [68] in combination with FlowSOM [61] for identifying the major canonical subsets defined by the HIMC manual gating template. To effectively enable analysis with an unsupervised algorithm pipeline, settings for both UMAP and clustering need to be calibrated for the number of events and complexity of the panel, and settings from one technology are transferrable to the other. It is important to increase the number of clusters beyond the estimated number of populations to ensure each population is clustered appropriately and account for small clusters, such as the innate lymphoid cells (ILCs) identifiable in this panel. It should also be noted that differences in the pre-pipeline cleanup steps, such as doublet and live/dead discrimination, mean that some unknown (unassigned) populations may differ between the two technologies.

The UMAP of the clusters displaying the canonical subsets described in the previous two approaches is presented for the FSFC (Figure 8A) and MC (Figure 8B) data. The identification was highly conserved between the two platforms for all the major subsets: $CD4^+$ subsets including $CD45RA^+$ and $CD45RA^-$ T regs, CD8 subsets, B cells (and plasmablasts), TCRγδ, NKs, monocytes, DCs, pDCs, Basophils, and ILCs. UMAP was able to separate the samples from each platform into two dimensional representations that contained nearly equivalent groups of events that conserve the global structure present in the datasets. For example, $CD4^+$ NK T cells were next to the CD4 island, DCs proximity to pDCs is similar, Monocyte transition from Classical to Non-Classical is represented, and ILCs are very close to NKs (in the NK island) in both datasets. (Figure 8A,B) A marker expression level heatmap comparison of these subsets is shown in Figure 8C. Overall, the heatmaps demonstrate highly reproducible data between the two platforms. In a few instances (examples highlighted in red boxes) there are differences between the two platforms. However, this is most likely due to differences in the frequencies of the positive events above background, that is, the median for the platform that has the lower frequency of positive events will be negatively impacted by the disproportionate contribution of the negative events to the median value. For example, differences can be seen in the expression of PD-1 on CD8 EM cells, but not on the expression of PD-1 on CD4 NKT cells, with the expression level of PD-1 on CD8 EM cells being higher on FSFC (red boxes). In this case the majority of events are positive for PD-1 on the NKT cells in both platforms, whereas the frequency of PD-1 positive events on the CD8 EM cells differs between the two platforms, with MC having a higher percentage of negative events contributing to having a lower median (dimmer shade of blue). Using a density UMAP, the abnormal NK population in donor 4395, which was noted in the two previous analysis approaches, can also be easily identified in both platforms (Figure 8D).

However, some differences in the pipeline results are visible. In the myeloid compartment, there are two $CD33^+CD14^{dim/-}$ populations in the FSFC data that are absent in the MC data, as well as an additional $CD56^{dim}CD16^-CD38^+$ population in the FSFC data (identified with an arrow in Figure 8A). Further inspection revealed the lower resolution of the myeloid markers CD14, CD16, and CD33 in the MC data made assigning them to a known population more difficult. These differences are consistent with the observations made when utilizing the other data analysis approaches described above. Examples of density UMAPs of markers where differences in the AOF values were found in previous analyses (CD127, CCR6, CD38, CXCR3, CD57, CD45RA, PD-1, and ICOS) are also displayed in Figure S7.

4 | CONCLUSION AND DISCUSSION

For the most part, the qualitative and quantitative results obtained in the two platforms, using multiple complimentary analysis approaches, are comparable. However, some differences were noted, and these were associated with differences in the resolution of the markers used to identify the monocytes and markers expressed at very low levels in certain donors.

Differences in marker resolution can be related to differences in clone performance, or if using the same clone, differences in performance between the reagents used in MC versus FSFC. Ideally, all clones should have been kept consistent across markers but there were constraints at the time when the study was done in the availability of fluorochrome-conjugated antibodies for some of the clones used in the MC panel, and overall when designing multicolor panels of this level of complexity.

An important factor to be able to assess comparability of the results obtained by these two different platforms was the use of different analysis strategies, from traditional manual gating to the use of sophisticated clustering algorithms and the inclusion of different metrics to assess resolution of each individual marker. All these analysis strategies are complimentary and, in our opinion, are needed to have a full assessment of the quality of the data and ability to robustly identify different cell subsets.

Based on these findings, it is feasible for a high-dimensional panel developed for MC to be converted to a fluorescence-based panel when utilizing FSFC, at least for surface immunophenotyping panels. Additional studies will need to be done to assess equivalency for applications requiring intracellular (cytokine, signaling) staining.

There are advantages and disadvantages to each of these technologies that need to be considered when using one or the other. For example, sample throughput is a major consideration for MC, while the need for bar coding is a consideration for FSFC, as this can be more challenging in the fluorescence space of a high-dimensional panel. Another important consideration is the technical expertise and maintenance required for operating a mass cytometer compared to a fluorescence based FSFC such as the Cytek® Aurora used in this study. Generally, signal spillover is a larger concern in FSFC than in MC, and therefore there is the need for accurate single-color controls. However, recent publications have reported that signal spillover due to issues such as metal oxidation, abundancy related spillover, and metal impurities can impact data quality and interpretation in MC [52,69]. Efforts have been employed using single metal bead based controls [52], unlabeled competitor antibody [69], or statistical approaches [70] for compensating crosstalk between channels to improve overall data quality.

The desire to sort the subpopulations identified through high-dimensional phenotyping for further downstream studies, such as single cell RNAseq (SCRNAseq) or functional studies, is common and possible using FSFC, but not MC. Other considerations based on the inherent differences in these technologies are presented in Table 1.

The important take home message from this evaluation is that panels previously designed for MC with 40 biomarkers, or less, can be effectively implemented utilizing FSFC with comparable results. It is also important to note, common to both technologies, the importance of careful experimental design and the use of appropriate controls to ensure the accuracy of the results [3, 35, 39, 40, 48, 50, 51, 56, 60, 62, 71–73]. With these technological tools, proper experimental design, and quality control, there is much to be learned using high-dimensional panels for assessing the immune network associated with cancer, health, and disease.

AUTHOR CONTRIBUTIONS

Maria C. Jaimes: Conceptualization (lead); data curation (lead); formal analysis (supporting); methodology (lead); project administration (lead); supervision (lead); visualization (supporting); writing – original draft (supporting); writing – review and editing (supporting). **Michael Leipold:** Conceptualization (supporting); data curation (supporting); formal analysis (supporting); methodology (supporting); visualization (supporting); writing – original draft (supporting); writing – review and editing (supporting). **Geoffrey Kraker:** Data curation (supporting); formal analysis (supporting); methodology (supporting); validation (supporting); visualization (supporting); writing – original draft (supporting). **El-ad David Amir:** Conceptualization (supporting); data curation (supporting); formal analysis (equal); methodology (supporting); validation (supporting); visualization (supporting); writing – original draft (supporting). **Holden Maecker:** Conceptualization (supporting); methodology (supporting); writing – original draft (supporting); writing – review and editing (supporting). **Joanne Lannigan:** Data curation (equal); formal analysis (equal); methodology (supporting); project administration (equal); validation (equal); visualization (equal); writing – original draft (equal); writing – review and editing (equal).

ACKNOWLEDGMENTS

The authors wish to thank James Wei and Erin Lawrence for their assistance in generating figures for the manuscript, and Patrick Duncker for his critical review of the manuscript.

CONFLICT OF INTEREST

Maria C. Jaimes and Geoffrey Kraker are employees of Cytek Biosciences, the manufacturer of the Aurora FSFC used in this study. Joanne Lannigan is a paid consultant for Cytek Biosciences, the manufacturer of the Aurora FSFC used in this study. El-ad Amir is the Founder and CEO of Astrolabe Diagnostics, a medical diagnostics software company that provided cloud-based cytometry analysis services for this study. Holden Maecker serves on the Scientific Advisory Board of Cytek Biosciences.

PEER REVIEW

The peer review history for this article is available at https://publons.com/publon/10.1002/cyto.a.24565.

ORCID

Michael Leipold https://orcid.org/0000-0001-5389-0906

Joanne Lannigan https://orcid.org/0000-0002-3981-8681

REFERENCES

1. Filipovic I, Sönnerborg I, Strunz B, Friberg D, Cornillet M, Hertwig L, et al. 29-color flow cytometry: Unraveling human liver NK cell repertoire diversity. Front Immunol. 2019;10:2692.
2. Park LM, Lannigan J, Jaimes MC. OMIP-069: Forty-color full spectrum flow cytometry panel for deep immunophenotyping of major cell subsets in human peripheral blood. Cytometry A. 2020;97:1044–51.
3. Mair F, Tyznik AJ. High-dimensional immunophenotyping with fluorescence-based cytometry: A practical guidebook. Methods Mol Biol. 2019;2032:1–29.
4. Farkona S, Diamandis EP, Blasutig IM. Cancer immunotherapy: The beginning of the end of cancer? BMC Med. 2016;14:73.
5. Gajewski TF. Cancer immunotherapy. Mol Oncol. 2012;6:242–50.
6. Makkouk A, Weiner GJ. Cancer immunotherapy and breaking immune tolerance: new approaches to an old challenge. Cancer Res. 2015;75:5–10.
7. Tang H, Qiao J, Fu Y-X. Immunotherapy and tumor microenvironment. Cancer Lett. 2016;370:85–90.
8. Daud AI, Loo K, Pauli ML, Sanchez-Rodriguez R, Sandoval PM, Taravati K, et al. Tumor immune profiling predicts response to anti-PD-1 therapy in human melanoma. J Clin Invest. 2016;126:3447–52.
9. Hartmann FJ, Babdor J, Gherardini PF, Amir E-AD, Jones K, Sahaf B, et al. Comprehensive immune monitoring of clinical trials to advance human immunotherapy. Cell Rep. 2019;28:819–31.
10. Li Z, Hu J, Qin Z, Tao Y, Lai Z, Wang Q, et al. High-dimensional single-cell proteomics analysis reveals the landscape of immune cells and stem-like cells in renal tumors. J Clin Lab Anal. 2019;34:e23155.

11. Quandt D, Dieter Zucht H, Amann A, Wulf-Goldenberg A, Borrebaeck C, Cannarile M, et al. Implementing liquid biopsies into clinical decision making for cancer immunotherapy. Oncotarget. 2017;8:48507–20.
12. Yuan J, Hegde PS, Clynes R, Foukas PG, Harari A, Kleen TO, et al. Novel technologies and emerging biomarkers for personalized cancer immunotherapy. J Immunother Cancer. 2016;4:3.
13. Coosemans A, Vankerckhoven A, Baert T, Boon L, Ruts H, Riva M, et al. Combining conventional therapy with immunotherapy: a risky business? Eur J Cancer. 2019;113:41–4.
14. Niewold P, Ashhurst TM, Smith AL, King NJC. Evaluating spectral cytometry for immune profiling in viral disease. Cytometry A. 2020; 97:1165–79.
15. Krieg C, Nowicka M, Guglietta S, Schindler S, Hartmann FJ, Weber LM, et al. High-dimensional single-cell analysis predicts response to anti-PD-1 immunotherapy. Nat Med. 2018;24:144–53.
16. Maleki Vareki S, Garrigós C, Duran I. Biomarkers of response to PD-1/PD-L1 inhibition. Crit Rev Oncol Hematol. 2017;116:116–24.
17. Reeves PM, Sluder AE, Paul SR, Scholzen A, Kashiwagi S, Poznansky MC. Application and utility of mass cytometry in vaccine development. FASEB J. 2018;32:5–15.
18. Jensen HA, Wnek R. Analytical performance of a25-marker spectral cytometry immune monitoring assay in peripheral blood. Cytometry. 2020;99:180–93.
19. Chattopadhyay PK, Gierahn TM, Roederer M, Love JC. Single-cell technologies for monitoring immune systems. Nat Immunol. 2014;15: 128–35.
20. Galli E, Friebel E, Ingelfinger F, Unger S, Núñez NG, Becher B. The end of omics? High dimensional single cell analysis in precision medicine. Eur J Immunol. 2019;49:212–20.
21. Yang L, George J, Wang J. Deep profiling of cellular heterogeneity by emerging single-cell proteomic technologies. Proteomics. 2019;20: e1900226.
22. Bonilla DL, Reinin G, Chua E. Full spectrum flow cytometry as a powerful technology for cancer immunotherapy research. Front Mol Biosci. 2020;7:612801.
23. Chattopadhyay PK, Winters AF, Lomas WE, Laino AS, Woods DM. High-parameter single-cell analysis. Annu Rev Anal Chem. 2019;12: 411–30.
24. Danova M, Torchio M, Comolli G, Sbrana A, Antonuzzo A, Mazzini G. The role of automated cytometry in the new era of cancer immunotherapy. Mol Clin Oncol. 2018;9:355–61.
25. Greenplate AR, Johnson DB, Ferrell PB, Irish JM. Systems immune monitoring in cancer therapy. Eur J Cancer. 2016;61:77–84.
26. Holmberg-Thyden S, Grønbæk K, Gang AO, El Fassi D, Hadrup SR. A user's guide to multicolor flow cytometry panels for comprehensive immune profiling. Anal Biochem. 2021;627:114210.
27. Bandura DR, Baranov VI, Ornatsky OI, Antonov A, Kinach R, Lou X, et al. Mass cytometry: technique for real time single cell multitarget immunoassay based on inductively coupled plasma time-of-flight mass spectrometry. Anal Chem. 2009;81:6813–22.
28. Ornatsky O, Bandura D, Baranov V, Nitz M, Winnik MA, Tanner S. Highly multiparametric analysis by mass cytometry. J Immunol Methods. 2010;361:1–20.
29. Atkuri KR, Stevens JC, Neubert H. Mass cytometry: a highly multiplexed single-cell technology for advancing drug development. Drug Metab Dispos. 2015;43:227–33.
30. Gadalla R, Noamani B, MacLeod BL, Dickson RJ, Guo M, Xu W, et al. Validation of cytof against flow cytometry for immunological studies and monitoring of human cancer clinical trials. Front Oncol. 2019; 9:415.
31. Irish JM, Doxie DB. High-dimensional single-cell cancer biology. Curr Top Microbiol Immunol. 2014;377:1–21.
32. Maby P, Corneau A, Galon J. Phenotyping of tumor infiltrating immune cells using mass-cytometry (CyTOF). Methods Enzymol. 2020;632:339–68.
33. O'Boyle KC, Ohtani T, Manne S, Bengsch B, Henrickson SE, Wherry EJ, et al. Exploration of T-cell diversity using mass cytometry. Methods Mol Biol. 2020;2111:1–20.
34. Maecker HT, Harari A. Immune monitoring technology primer: flow and mass cytometry. J Immunother Cancer. 2015;3:44.
35. Lee BH, Rahman AH. Acquisition, processing, and quality control of mass cytometry data. In: HM MG, Ashhurst TM, editors. Mass cytometry: Methods and protocols. Methods in Molecular Biology. Volume 1989. New York, NY: Humana Press; 2019. p. 13–33.
36. Nolan JP, Condello D. Spectral flow cytometry. Curr Protoc Cytom. 2013;63:27.
37. Sanders CK, Mourant JR. Advantages of full spectrum flow cytometry. J Biomed Opt. 2013;18:037004.
38. Schmutz S, Valente M, Cumano A, Novault S. Spectral cytometry has unique properties allowing multicolor analysis of cell suspensions isolated from solid tissues. PLoS One. 2016;11:e0159961.
39. Ferrer-Font L, Small SJ, Lewer B, Pilkington KR, Johnston LK, Park LM, et al. Panel optimization for high-dimensional immunophenotyping assays using full-spectrum flow cytometry. Curr Protoc. 2021;1:e222.
40. Ferrer-Font L, Pellefigues C, Mayer JU, Small SJ, Jaimes MC, Price KM. Panel design and optimization for high-dimensional immunophenotyping assays using spectral flow cytometry. Curr Protoc Cytom. 2020;92:e70.
41. Futamura K, Sekino M, Hata A, Ikebuchi R, Nakanishi Y, Egawa G, et al. Novel full-spectral flow cytometry with multiple spectrally-adjacent fluorescent proteins and fluorochromes and visualization of in vivo cellular movement. Cytometry A. 2015;87:830–42.
42. Grégori G, Patsekin V, Rajwa B, Jones J, Ragheb K, Holdman C, et al. Hyperspectral cytometry at the single-cell level using a 32-channel photodetector. Cytometry A. 2012;81:35–44.
43. Alpert A, Pickman Y, Leipold M, Rosenberg-Hasson Y, Ji X, Gaujoux R, et al. A clinically meaningful metric of immune age derived from high-dimensional longitudinal monitoring. Nat Med. 2019;25: 487–95.
44. Yabu JM, Siebert JC, Maecker HT. Immune profiles to predict response to desensitization therapy in highly HLA-sensitized kidney transplant candidates. PLoS One. 2016;11:e0153355.
45. Mitra-Kaushik S, Mehta-Damani A, Stewart JJ, Green C, Litwin V, Gonneau C. The evolution of single-cell analysis and utility in drug development. AAPS J. 2021;23:98.
46. Ferrer-Font L, Mayer JU, Old S, Hermans IF, Irish J, Price KM. High-dimensional data analysis algorithms yield comparable results for mass cytometry and spectral flow cytometry data. Cytometry A. 2020;97:824–31.
47. Finak G, Langweiler M, Jaimes M, Malek M, Taghiyar J, Korin Y, et al. Standardizing flow cytometry immunophenotyping analysis from the human immunophenotyping consortium. Sci Rep. 2016;6:20686.
48. Tricot S, Meyrand M, Sammicheli C, Elhmouzi-Younes J, Corneau A, Bertholet S, et al. Evaluating the efficiency of isotope transmission for improved panel design and a comparison of the detection sensitivities of mass cytometer instruments. Cytometry A. 2015;87: 357–68.
49. Olsen LR, Leipold MD, Pedersen CB, Maecker HT. The anatomy of single cell mass cytometry data. Cytometry A. 2019;95:156–72.
50. Nguyen R, Perfetto S, Mahnke YD, Chattopadhyay P, Roederer M. Quantifying spillover spreading for comparing instrument performance and aiding in multicolor panel design. Cytometry A. 2013;83: 306–15.
51. Ferrer-Font L, Pellefigues C, Mayer JU, Small S, Jaimes MC, Price KM. Design and optimization protocol for high-dimensional Immunophenotyping assays using spectral flow cytometry. Curr Protoc Cytom. 2020;92(1):e70.
52. Chevrier S, Crowell HL, Zanotelli VRT, Engler S, Robinson MD, Bodenmiller B. Compensation of signal spillover in suspension and imaging mass cytometry. Cell Syst. 2018;6:612–20.

53. Budzinski L, Schulz AR, Baumgart S, Burns T, Rose T, Hirseland H, et al. Osmium-labeled microspheres for bead-based assays in mass cytometry. J Immunol. 2019;202:3103–12.
54. Amir E-AD, Lee B, Badoual P, Gordon M, Guo XV, Merad M, et al. Development of a comprehensive antibody staining database using a standardized analytics pipeline. Front Immunol. 2019;10:1315.
55. Hahne F, LeMeur N, Brinkman RR, Ellis B, Haaland P, Sarkar D, et al. flowCore: A bioconductor package for high throughput flow cytometry. BMC Bioinfo. 2009;10:106.
56. Amir E-AD, Guo XV, Mayovska O, Rahman AH. Average overlap frequency: a simple metric to evaluate staining quality and community identification in high dimensional mass cytometry experiments. J Immunol Methods. 2018;453:20–9.
57. Meskas J, Wang S, Brinkman R. flowCut — An R package for precise and accurate automated removal of outlier events and flagging of files based on time versus fluorescence analysis. BioRxiv. 2020.
58. Sainburg T, McInnes L, Gentner TQ. Parametric UMAP embeddings for representation and semisupervised learning. Neural Comput. 2021;1–27:1–27.
59. Do VH, Canzar S. A generalization of t-SNE and UMAP to single-cell multimodal omics. Genome Biol. 2021;22:130.
60. Rybakowska P, Van Gassen S, Quintelier K, Saeys Y, Alarcón-Riquelme ME, Marañón C. Data processing workflow for large-scale immune monitoring studies by mass cytometry. Comput Struct Biotechnol J. 2021;19:3160–75.
61. Van Gassen S, Callebaut B, Van Helden MJ, Lambrecht BN, Demeester P, Dhaene T, et al. FlowSOM: using self-organizing maps for visualization and interpretation of cytometry data. Cytometry A. 2015;87:636–45.
62. Takahashi C, Au-Yeung A, Fuh F, Ramirez-Montagut T, Bolen C, Mathews W, et al. Mass cytometry panel optimization through the designed distribution of signal interference. Cytometry A. 2017;91:39–47.
63. Roederer M. Distributions of autofluorescence after compensation: Be panglossian, fret not. Cytometry A. 2016;89:398–402.
64. Lee H, Sun Y, Patti-Diaz L, Hedrick M, Ehrhardt AG. High-throughput analysis of clinical flow cytometry data by automated gating. Bioinform Biol Insights. 2019;13:1177932219838851.
65. Newman JRS, Ghaemmaghami S, Ihmels J, Breslow DK, Noble M, DeRisi JL, et al. Single-cell proteomic analysis of S. cerevisiae reveals the architecture of biological noise. Nature. 2006;441:840–6.
66. Nowicka M, Krieg C, Crowell HL, Weber LM, Hartmann FJ, Guglietta S, et al. CyTOF workflow: Differential discovery in high-throughput high-dimensional cytometry datasets. [version 3; peer review: 2 approved]. F1000Res. 2017;6:748.
67. Brummelman J, Haftmann C, Núñez NG, Alvisi G, Mazza EMC, Becher B, et al. Development, application and computational analysis of high-dimensional fluorescent antibody panels for single-cell flow cytometry. Nat Protoc. 2019;14:1946–69.
68. Becht E, McInnes L, Healy J, Dutertre C-A, Kwok IWH, Ng LG, et al. Dimensionality reduction for visualizing single-cell data using UMAP. Nat Biotechnol. 2018;37:38–44.
69. Sekhri P, Kim MY, Behbehani GK. Unlabeled competitor antibody to reduce nonlinear signal spillover in mass cytometry. Cytometry A. 2019;95:898–909.
70. Miao Q, Wang F, Dou J, Iqbal R, Muftuoglu M, Basar R, et al. Ab initio spillover compensation in mass cytometry data. Cytometry A. 2021;99:899–909.
71. Sahaf B, Pichavant M, Lee BH, Duault C, Thrash EM, Davila M, et al. Immune profiling mass cytometry assay harmonization: multicenter experience from CIMAC-CIDC. Clin Cancer Res. 2021;27:5062–71.
72. Lee BH, Rahman AH. Acquisition, processing, and quality control of mass cytometry data. Methods Mol Biol. 2019;1989:13–31.
73. Leipold MD, Maecker HT. Mass cytometry: protocol for daily tuning and running cell samples on a CyTOF mass cytometer. J Vis Exp. 2012;(69):e4398.

SUPPORTING INFORMATION

Additional supporting information may be found in the online version of the article at the publisher's website.

How to cite this article: Jaimes MC, Leipold M, Kraker G, Amir E, Maecker H, Lannigan J. Full spectrum flow cytometry and mass cytometry: A 32-marker panel comparison. Cytometry. 2022;101(11):942–59. https://doi.org/10.1002/cyto.a.24565